

Autonomous Repair Mechanism of Creep Damage in Fe-Au and Fe-Au-B-N Alloys



S. ZHANG, C. KWAKERNAAK, F.D. TICHELAAR, W.G. SLOOF, M. KUZMINA, M. HERBIG, D. RAABE, E. BRÜCK, S. VAN DER ZWAAG, and N.H. VAN DIJK

The autonomous repair mechanism of creep cavitation during high-temperature deformation has been investigated in Fe-Au and Fe-Au-B-N alloys. Combined electron-microscopy techniques and atom probe tomography reveal how the improved creep properties result from Au precipitation within the creep cavities, preferentially formed on grain boundaries oriented perpendicular to the applied stress. The selective precipitation of Au atoms at the free creep cavity surface results in pore filling, and thereby, autonomous repair of the creep damage. The large difference in atomic size between the Au and Fe strongly hampers the nucleation of precipitates in the matrix. As a result, the matrix acts as a reservoir for the supersaturated solute until damage occurs. Grain boundaries and dislocations are found to act as fast transport routes for solute gold from the matrix to the creep cavities. The mechanism responsible for the self-healing can be characterized by a simple model for cavity growth and cavity filling.

DOI: 10.1007/s11661-015-3169-9

© The Author(s) 2015. This article is published with open access at Springerlink.com

I. INTRODUCTION

CORROSION-RESISTANT steels serve as key alloys in multiple high-temperature applications found in for example power plant components. When these steel components are operated at high temperatures for long times, they can show premature creep failure, arising from the formation, growth, and coalescence of creep cavities located at grain boundaries into macroscopic cracks.^[1,2] Extensive research has focussed on identifying the metallurgical processes that help preventing the formation of this pore-related high-temperature creep damage.^[3–5]

A viable alternative to these established approaches to avoid premature creep damage can be achieved by incorporation self-healing capabilities in these steels. As recently demonstrated, self-healing of damage can significantly enhance the component lifetime for a wide range of materials, including metals.^[6–9] For austenitic stainless steels, Shinya and coworkers have recently

proposed that creep damage can be healed when the alloys were compositionally modified with additions of Cu and additions of both B and N.^[10–13] The resulting enhanced creep resistance was proposed to be attributed to dynamic precipitation of either Cu or BN at the crack surface. In our previous work, copper precipitation was indeed observed at open-volume defects in solutionized Fe-Cu and Fe-Cu-B-N model alloys.^[14–16] However, Cu precipitation at deformation-induced defects was found to be relatively weak as spherical Cu precipitates are simultaneously formed inside the matrix.

In order to preserve the driving force for segregation from the matrix, but at the same time to suppress undesired precipitation inside the matrix, we substituted Au for Cu as the healing element. Earlier studies^[17,18] confirmed that Au atoms in Fe-Au alloys show a pronounced preference to segregate to dislocations. In our earlier investigations on thermal aging of pre-deformed high-purity Fe-Au and Fe-Au-B-N alloys (with about 1 at. pct Au) a clear defect-induced Au precipitation was observed.^[19–21] The exclusive segregation of Au on deformation-induced internal defects makes Au an excellent healing agent for creep damage in a ferrous matrix. Owing to the large difference in atomic radius between Au and Fe ($r_{\text{Au}}/r_{\text{Fe}} = 1.13$) nucleation of precipitates inside the alloy matrix is expected to be low as a result of the strain energy associated with the precipitate nucleus. For a solutionized Fe-Au alloy (solid solution), the solute gold atoms thus remain in the dissolved state until internal defects in the form of creep cavities (providing a free internal surface and open volume) are formed. This mechanism then triggers precipitate nucleation and subsequent transfer of solute Au atoms toward the defect site, resulting in precipitate growth. For the Fe-Au system, a strong driving force for Au precipitation at cavity surfaces is expected,

S. ZHANG, Ph.D. Student, E. BRÜCK, Professor, and N.H. VAN DIJK, Researcher, are with the Fundamental Aspects of Materials and Energy, Faculty of Applied Sciences, Delft University of Technology, Mekelweg 15, 2629 JB Delft, The Netherlands. Contact e-mail: n.h.vandijk@tudelft.nl C. KWAKERNAAK, Research Assistant, and W.G. SLOOF, Researcher, are with the Department of Materials Science and Engineering, Delft University of Technology, Mekelweg 2, 2628 CD Delft, The Netherlands. F.D. TICHELAAR, Researcher, is with the Kavli Institute of Nanoscience, National Centre for HREM, Delft University of Technology, Lorentzweg 1, 2628 CJ Delft, The Netherlands. M. KUZMINA, Ph.D. Student, M. HERBIG, Researcher, and D. RAABE, Professor, are with the Max-Planck-Institut für Eisenforschung GmbH, Max-Planck-Straße 1, 40237 Düsseldorf, Germany. S. VANDER ZWAAG, Professor, is with the Novel Aerospace Materials group, Faculty of Aerospace Engineering, Delft University of Technology, Kluyverweg 1, 2629 HS Delft, The Netherlands.

Manuscript submitted April 10, 2015.

Article published online October 6, 2015

considering our previous X-ray photoelectron spectroscopy (XPS) observations, which revealed that Au atoms have a strong tendency to segregate to a free surface.^[20]

In a recent paper, we reported on the improved creep lifetime in the Fe-Au alloy compared to a Fe-Cu alloy.^[22] In the present study, we substantially expanded the work on this system and clarify the autonomous repair mechanism responsible for the improved creep properties by studying the microstructures and pore-filling mechanism in detail, using both high-resolution structural and chemical analytic probes. In addition, the role of interstitial boron and nitrogen atoms is investigated by comparing the properties of Fe-Au and Fe-Au-B-N alloys. Although the effects of precipitation on the creep behavior have been studied by many groups for different types of steels,^[23–28] these studies so far exclusively focused on the interaction between the evolution in precipitate size distribution and the strength of the material during high-temperature creep. Here, site-selective precipitation during creep is studied in the context of self-healing of creep damage in order to improve the creep lifetime. To better understand the mechanism responsible for pore filling and thus material healing, the interplay between creep cavity formation and site-selective precipitation of Au within these cavities is studied in detail for solutionized Fe-Au and Fe-Au-B-N alloys. Electron probe micro-analysis (EPMA) and atom probe tomography (APT) are used to investigate the elemental diffusion pathways during creep on a coarse and fine scale, respectively, and thereby characterize local chemical compositions and the healing kinetics.

II. EXPERIMENTAL

The composition of the studied Fe-Au and Fe-Au-B-N alloys (produced by Goodfellow) is shown in Table I. A small amount of Ce was added to the alloys to bind trace impurities of sulfur (<0.002 wt pct).^[12,13] Mechanical testing was conducted by using miniaturized creep specimens which were of dog-bone type shape with a gauge length of 12.5 mm, a width of 6 mm, and a thickness of 0.5 mm (cross section of 3 mm² for creep loading), machined by spark erosion from rolled sheet material. To fully dissolve all solute atoms, the samples were solution heat treated for 5 hours at 1141 K (868 °C) for the Fe-Au and Fe-Au-B-N alloys in evacuated silica tubes filled with 200 mbar ultra-high purity argon, followed by a rapid water quench. This heat treatment results in a (supersaturated) solid solution of the alloys without segregation and a fully equi-axed ferritic structure. The average grain size amounts to 57 ± 8 and 24 ± 5 μm for the Fe-Au alloy

(the alloy was produced in the form of two separate sheets) and 35 ± 8 μm for the Fe-Au-B-N alloy.

Creep tests were performed using an Instron testing machine (5560 series with a 1 kN load cell) equipped with a home-built creep test module operating at high temperatures. To avoid surface oxidation of samples, the miniature creep tester works under high vacuum conditions (<1 × 10⁻⁴ mbar). The creep tests were conducted at a constant temperature of 823 K (550 °C) and at constant creep loads corresponding to applied stresses ranging from 60 to 133 MPa. In the binary Fe-Au alloy, the equilibrium solubility of Au in the Fe-rich phase is negligible at 823 K (550 °C). The homogenized solute concentration of about 1 at. pct Au provides a strong chemical driving force for segregation and precipitation.

Microstructures were analyzed with a scanning electron microscope (JEOL JSM 6500F) equipped with an Autrata back-scattered electron detector and an electron back-scattering diffraction (EBSD) system employing an Oxford-HKL Nordlys II detector. Micrographs were taken with an electron beam energy of 10 kV and 15 keV. The EBSD patterns were acquired with an electron beam energy of 20 keV and a beam current of 600 pA. The microstructure analysis was performed in the uniform elongation portion of the samples (except for the analysis of the fracture surface). Transmission electron microscopy (TEM) measurements were performed using a Tecnai F20ST/STEM instrument operated at 200 keV.

Electron Probe Micro-analysis (EPMA) measurements were performed with a JEOL JXA 8900R microprobe using an electron beam with energy of 10 keV and beam current of 50 nA employing wavelength dispersive spectrometry (WDS). The obtained intensity ratios were processed using a matrix correction program CITZAF.^[29] An air-jet decontamination device was used to remove *in situ* generated surface carbon.

Atom probe specimens were prepared site-specifically using a FEI Helios NanoLab 600i dual-beam FIB/SEM instrument. The specimens were extracted from the surface of the bulk material by standard FIB lift-out procedures, deposited on a commercial Si tip array and then sharpened to tip radii of <100 nm, followed by a cleaning procedure as described by Thompson^[30] and analyzed by APT. APT characterization was conducted on a LEAP 3000X HR instrument (Cameca), at a base temperature of 70 ± 4 K, operated in laser-pulsed mode (wavelength 532 nm; pulse repetition rate: 200 kHz) with 0.2 nJ pulse energy in a voltage range starting from 4 kV. Reconstruction was carried out using commercial software (Cameca IVAS[®]) following the protocol introduced by Geiser and coworkers.^[31] In the APT mass spectrum peaks at 14.5 and 15 Da indicating the presence of Si and a peak at 17 Da indicating the

Table I. The Chemical Composition of the Studied Alloys (in Weight Percent) with Balance Iron

Alloy	Au	B	N	C	Ce
Fe-Au	2.87	<0.01	0.0085	0.0008	0.015
Fe-Au-B-N	2.83	0.05	0.0156	0.0003	0.015

presence of S were absent. The peaks at 14 and 16 Da were thus entirely assigned to N and O, respectively. The Gibbsian interface excess was quantified using ladder diagrams^[32] along cylindrical regions of interest with an average diameter of 30 nm.

III. RESULTS

A. Creep Behavior at Constant Stress

Figure 1 shows the strain-time curves at constant stress for the solutionized Fe-Au and Fe-Au-B-N alloys. The observed creep curves show the conventional stages including a rapid initial strain development stage (stage I), followed by a regime with a nearly constant strain rate indicating stationary creep (stage II) until strain acceleration sets in near the failure regime (stage III). As most of the creep life is spent in the second creep stage (stage II), the creep lifetime of engineering alloys is dominated by the nearly constant secondary creep rate.

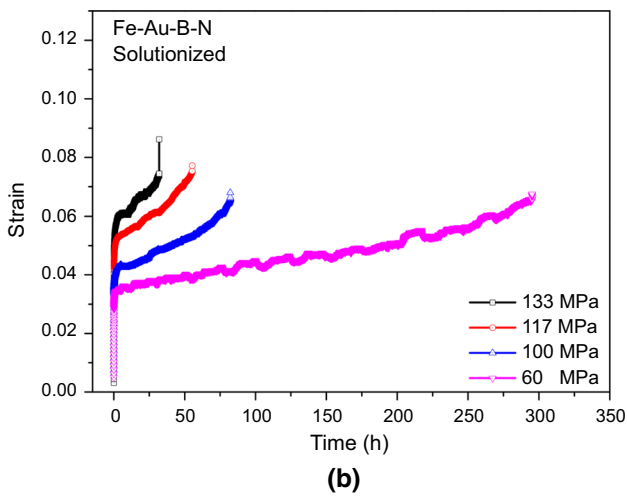
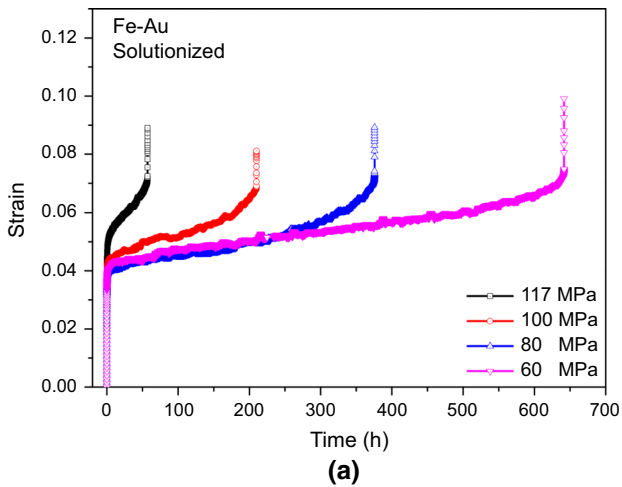


Fig. 1—Creep curves at constant stress for (a) the solutionized Fe-Au alloy,^[22] (b) the solutionized Fe-Au-B-N alloy during creep at 823 K (550 °C). The average grain size is 57 μm for the Fe-Au alloy and 35 μm for the Fe-Au-B-N alloy.

This steady-state strain rate strongly depends on the temperature T , the applied stress σ , and the grain size d . In the secondary creep regime, the creep rate can be approximated using the Sherby–Dorn equation^[33]:

$$\dot{\epsilon}_s = Ad^m \sigma^n \exp\left(-\frac{Q}{RT}\right), \quad [1]$$

where A is a microstructure-dependent constant, Q is an apparent activation barrier, m is the grain size exponent and n is the stress exponent.

Figure 2(a) shows the Norton plots for the Fe-Au and Fe-Au-B-N alloys during creep at 823 K (550 °C). A stress exponent of $n \approx 2$ is observed for both the Fe-Au and Fe-Au-B-N alloys in the stress regime between 60 and 100 MPa. The deformation mechanism is a combination of volume diffusion and dislocation motion modes.^[34–36] Additional creep tests on the solutionised Fe-Au alloy at a load of 100 MPa for temperatures of 808 K, 823 K, 848 K (535 °C, 550 °C, and 575 °C) resulted in correspondingly higher steady-state creep

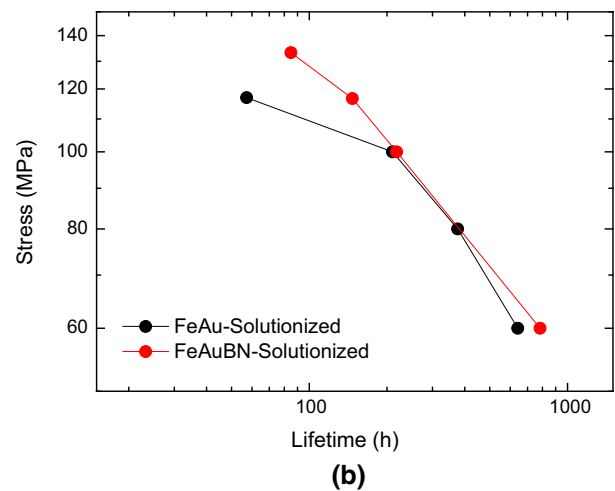
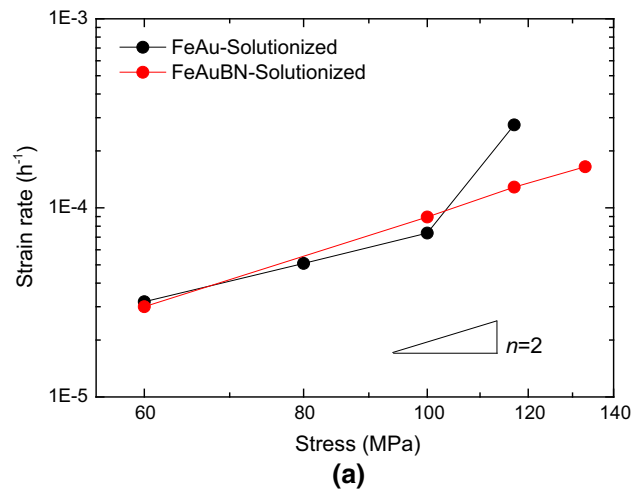


Fig. 2—Variation of (a) steady state strain rate and (b) creep lifetime with applied stresses for the Fe-Au^[22] and Fe-Au-B-N alloys for creep at 823 K (550 °C). The strain rate and lifetime have been compensated for variations in grain size.

strain rates of $\dot{\epsilon}_s = 8.7 \times 10^{-9}$, 2.0×10^{-8} , $5.2 \times 10^{-8} \text{ s}^{-1}$, respectively. Using Eq. [1] an experimental activation energy of $Q = 257 \pm 15 \text{ kJ/mol}$ was obtained for the solutionized Fe-Au alloy, which is in close agreement with the activation energy that was reported for Au diffusion in bcc Fe.^[37] It is worth mentioning that the steady-state strain rate is influenced by the grain size for both the power-law and diffusional creep.^[33,38] The creep rate of the Fe-Au-B-N alloy has therefore been normalized to the average grain size of the Fe-Au alloy ($d = 57 \mu\text{m}$). According to Eq. [1] the creep rate depends on the grain size as $\dot{\epsilon}_s \propto d^m$, where $m = -2$ was deduced from the experimental data for the Fe-Au alloy with two different grain sizes of $57 \mu\text{m}$ (Figure 1) and $24 \mu\text{m}$ (not shown). Using this relation the experimental data for the strain rate of Fe-Au-B-N alloy could be scaled to the same grain size as for the Fe-Au alloy. Figure 2(b) shows the variation in creep lifetime as a function of the applied stress. At lower stress levels no obvious influence of the added B and N is observed on the creep lifetime of the Fe-Au alloy.

B. Microstructure After Creep

In Figure 3(a), the intergranular fracture surface is shown for the Fe-Au-B-N alloy after creep fracture at a load of 60 MPa and a temperature of 823 K (550 °C). Fracture occurred after 295 hour, as indicated in

Figure 1(b). At the locations indicated by the arrows, creep cavities and cracks are observed on the stress-affected grain boundaries. On the fracture surface a high concentration of Au precipitates (white regions) is observed, which confirms a preferred precipitation of Au at creep damage sites. In Figure 3(b) the microstructure of the Fe-Au alloy after creep at 117 MPa is shown. At the triple junctions, one grain boundary wedge crack labeled as (1) is completely filled, while another one labeled as (2) is partially filled with Au precipitates. Two parts of the grain boundary are studied in more detail in Figures 3(c) and (d): (1) a region with irregular-shaped Au precipitates without damage and (2) a region where the creep damage is partially filled with Au precipitates. The isolated Au ribbon in the region (1) is proposed to have fully filled previously formed creep damage, based on the irregular shape of the formed precipitates that reflects the morphology of the creep damage. It is worth noting that an Au-depleted region is formed along the grain boundary, reflected by the dark color. For region (2), the shape of the Au precipitates formed along the grain-boundaries cavities is again irregular and matches the geometry of the partly filled creep damage. This is explained by the preferential Au segregation to inner surfaces of the creep cavities and the subsequent continuous growth of precipitates within them. However, when the Au filling is slower than the cavity growth and coalescence rate only a partial healing effect is reached.

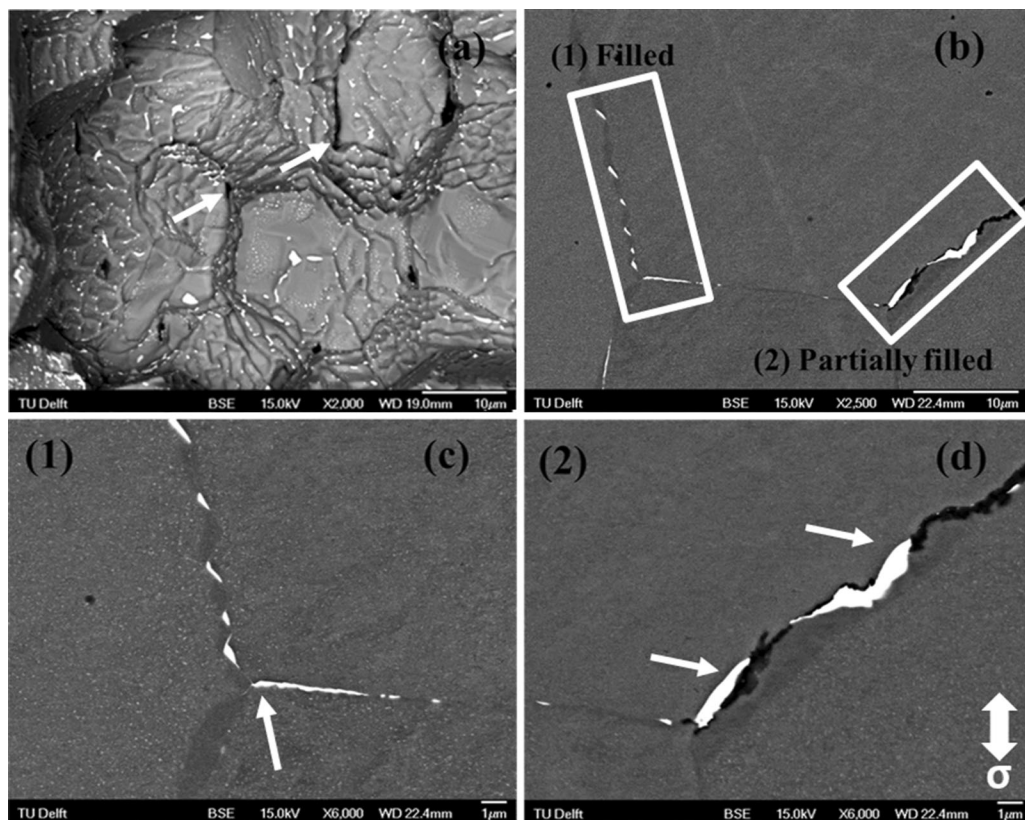


Fig. 3—(a) Fracture surface of the Fe-Au-B-N alloy after creep at 60 MPa, (b) Micrograph of filled and partially filled cavities and microcracks along grain boundaries, (c) and (d) the enlargement of the regions indicated as (1) and (2) in (b), respectively, for the Fe-Au alloy after creep at 117 MPa. The direction of the applied stress is indicated in the lower right corner. The creep experiments were performed at a temperature of 823 K (550 °C).

In Figure 4(a), the microstructure of the Fe-Au sample is shown after creep at a stress of 117 MPa. A close spatial correlation between the grain-boundary cavities and the Au precipitates is observed. Figure 4(b) shows the microstructure of the Fe-Au-B-N alloy after creep at a stress of 60 MPa. The distribution of Au precipitates is similar to that observed in the Fe-Au alloy, revealing a pronounced trend to form precipitates at locations that are strongest affected by the applied stress, namely, at grain boundaries perpendicular to the stress and at triple-point junctions. The depletion zone is generally smaller than observed for the Fe-Au alloy, despite a longer creep lifetime. This is consistent with the results obtained for pre-strained Fe-Au and Fe-Au-B-N alloys, where the addition of B and N was found to result in a deceleration of the Au precipitation kinetics.^[19,21] Figure 4(c) shows the distribution of Au precipitates along grain boundaries as a function of the misorientation angle θ between the grain boundary and the direction of the applied stress (note that the 2D projected grain boundary is considered in the SEM picture). The Au precipitation strongly increases for higher misorientation angles. Most of the Au precipitates are formed along the grain boundaries of which the planes are oriented perpendicular to the stress direction. As these are also the grain boundaries that are most likely to show creep damage under the applied stress, a clear correlation between creep damage and site-selective precipitation is observed.

In order to characterize the creep cavity formation and Au precipitation in more detail additional TEM experiments were performed. Figure 5 shows the microstructure of the fractured Fe-Au and Fe-Au-B-N samples after creep. In the TEM images nano-sized disk-shaped particles are observed to be uniformly

formed within the matrix. The presence of a Au-depletion zone close to the grain boundary is confirmed (Figure 5(a)). Coarse precipitates (>100 nm) are found along the grain boundaries (Figure 5(b)). Some particles are even interlinked to form micron-sized precipitates. The particles aligned along grain boundaries correspond to $\text{Au}_x\text{Fe}_{1-x}$ with a disordered *fcc* structure and a lattice parameter of $a = 4.04$ Å (see the CBED pattern obtained on particle *p1*, shown as the insert image in Figure 5(b)). As shown in Figure 5(c), some cavities are about to coalesce, which will ultimately lead to failure. The formation of Au particles on the cavity surface is also observed, as indicated by arrows in Figures 5(c) and (d). As shown in Figure 5(e) an orientation relation $\{220\}_{\text{AuFe}} \parallel \{002\}_{\alpha\text{-Fe}}$ is found between the *fcc* particle (AuFe) and the *bcc* matrix ($\alpha\text{-Fe}$). This orientation relationship was observed for many faceted precipitates at grain boundaries, with the facet plane oriented on $\{220\}_{\text{AuFe}}$ and $\{002\}_{\alpha\text{-Fe}}$. These planes have almost the same interplanar distance (1.44 Å for $\{220\}_{\text{AuFe}}$ and 1.43 Å for $\{002\}_{\alpha\text{-Fe}}$), consistent with a coherent interface. The close correlation between the presence of dislocations and the formation of disk-shaped Au precipitates is clearly illustrated in Figure 5(f). In agreement with previous aging experiments of pre-deformed samples^[19,21] we find that each disk-shaped precipitate is connected to a dislocation, confirming the heterogeneous nature of the nucleation of these precipitates.

Figure 6(a) shows the back-scatter SEM images of the Fe-Au alloy after creep at 90 MPa. A variation in Au precipitation is observed for grain boundaries that have the same orientation with respect to the stress. For example, the density of Au precipitates formed along the grain boundary between grains 2 and 3 is obviously

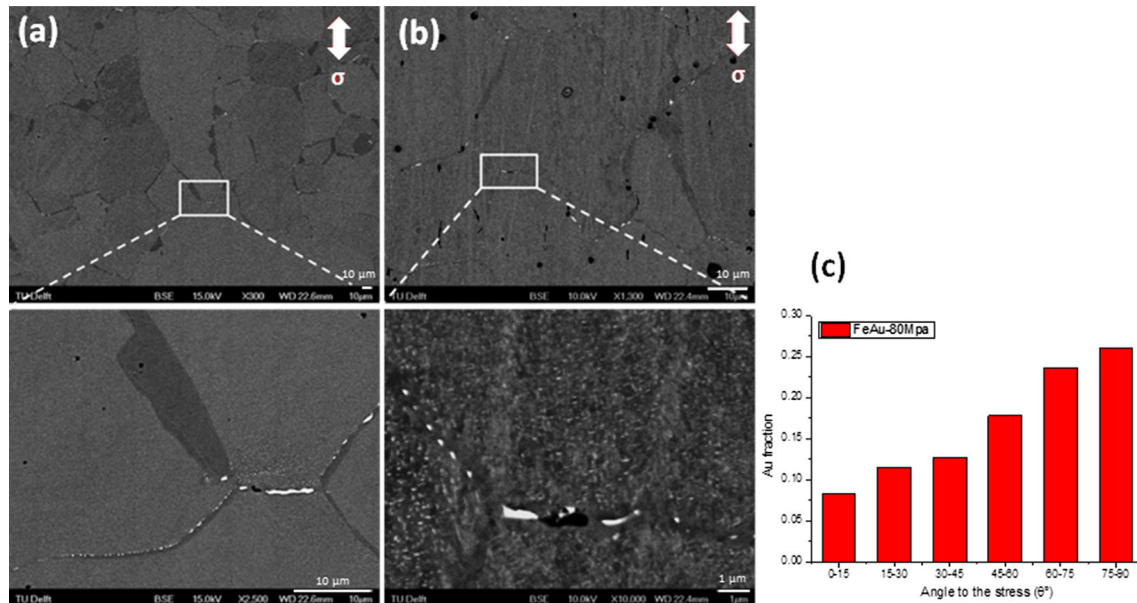


Fig. 4—SEM-backscattered electron images for (a) the Fe-Au alloy after creep at 117 MPa^[22] and (b) the Fe-Au-B-N alloy after creep at 60 MPa, (c) the fraction of Au precipitates along grain boundaries (GBs) as a function of the GB orientation angle to the stress direction for the Fe-Au after creep at 80 MPa. The considered GB orientation corresponds to the 2D projected plane normal in the SEM picture. The creep experiments were performed at a temperature of 823 K (550 °C).

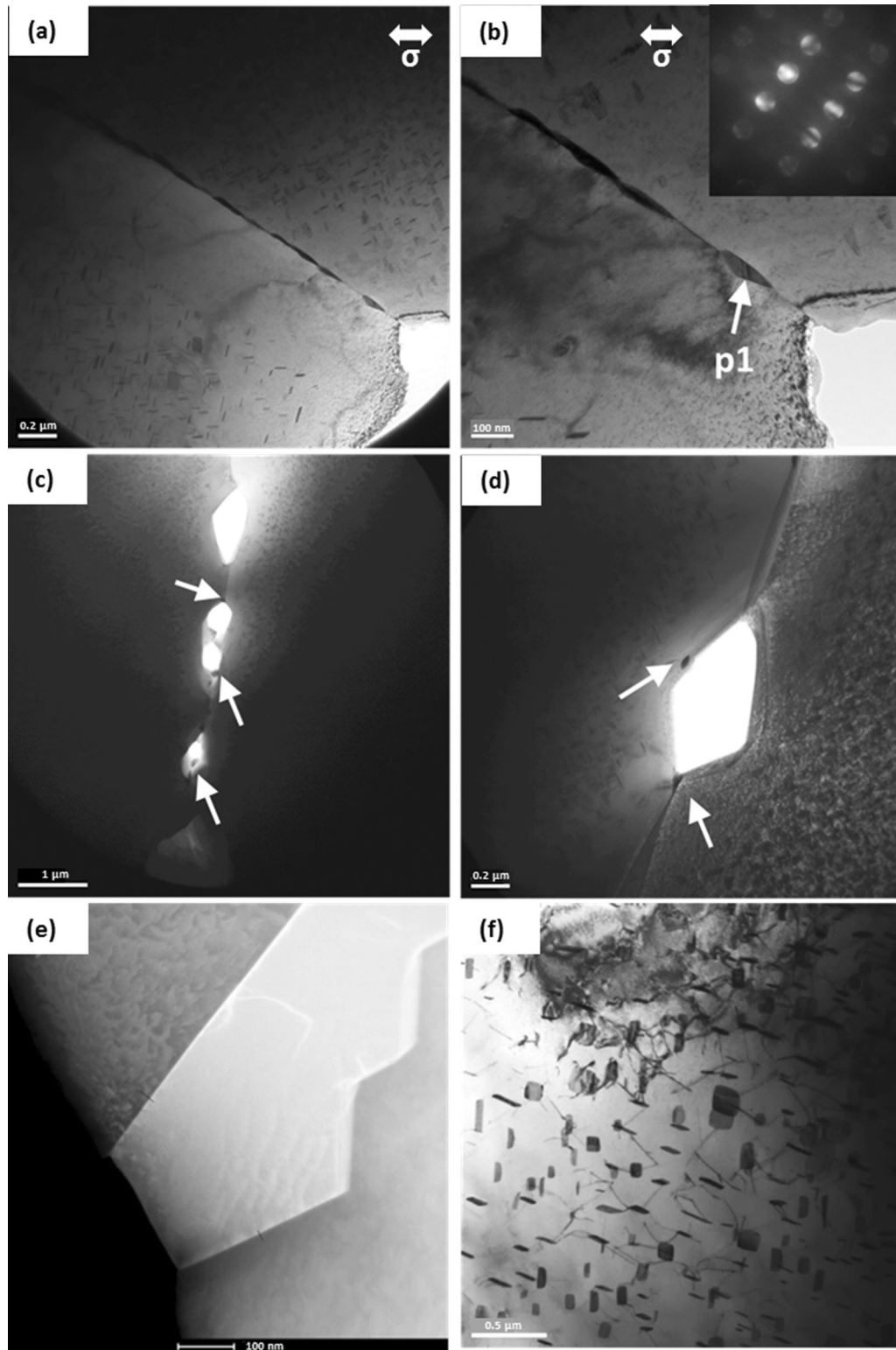


Fig. 5—TEM images of (a through d) the Fe-Au-B-N alloy after creep at 100 MPa and (e, f) the Fe-Au alloy after creep at 80 MPa. The insert image in (b) is the CBED pattern of particle 1 (p1). (a through d) and (f) were obtained in bright-field mode and (e) in STEM annular dark field mode. The creep experiments were performed at a temperature of 823 K (550 °C).

higher than that along the grain boundary between grains 3 and 4, even though the orientation of both GBs is very close ($\theta \approx 90$ deg). At high magnification

(Figure 6(b)), the creep cavitation is clearly observed along the boundary between grains 2 and 3. While the wedge crack at the triple-point junction is fully filled, the

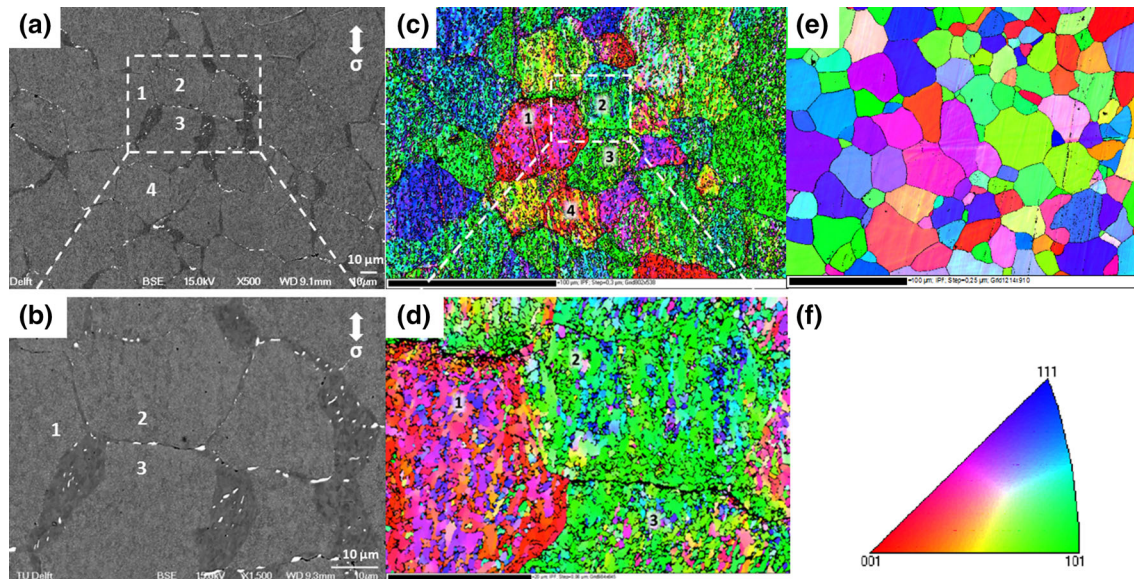


Fig. 6—(a, b) SEM-backscattered electron images and (c, d) orientation maps for the Fe-Au alloy after creep at 90 MPa and (e) for the solutionized Fe-Au alloy before creep with colors corresponding to the inverse pole figure (f) with respect to the sample surface normal.

grain boundary cavities are only partially filled with Au precipitates. To clarify the dependence of cavitation and precipitation on the nature of the grain boundary, EBSD measurements were performed at the same region, as shown in Figures 6(c) and (d). During creep a high density of subgrains is formed. These subgrains are absent in the initial microstructure, as shown in Figure 6(e), but were formed by the interaction of migrating creep induced dislocations.^[39] Within the uncertainty caused by the interference of the subgrain boundaries, we can see that the misorientation between grain 2 and 3 (GB₂₃) is smaller than between grain 3 and 4 (GB₃₄). Correspondingly, the amount of Au precipitates along GB₂₃ is higher than that along GB₃₄. This might indicate that Au precipitates are preferentially formed at low-angle grain boundaries. According to the interface damage function (IDF),^[40] the grain boundary cavitation depends on the orientation to the stress and the lattice misorientation. Creep cavitation was shown to have a tendency to occur at small-angle boundaries, while random high-angle boundaries are remarkably creep-damage resistant.^[40,41] SEM and EBSD measurements on the Fe-Au-B-N alloy after creep loading at 60 MPa gave similar results.

The Au diffusion pathways during creep were studied in more detail on a coarse scale using EPMA and on a near-atomic scale using APT. In Figure 7 the elemental concentration profiles of Au as measured by EPMA are shown for the Fe-Au alloy after creep loading at 90 MPa. As in the SEM images of Figures 3, 4 and 6 clear dark regions are observed that reflect Au-depleted zones. It is interesting to note that these regions are located in the vicinity of the grain boundaries that are aligned with the applied stress (in contrast to the perpendicular grain boundaries that are most sensitive to creep damage). This strongly suggests that the volume diffusion within the matrix is significantly faster

perpendicular to the applied load than along the load. To characterize the concentration profile of Au, scans along the lines marked in Figure 7(a) were performed. L1 crosses a dark region along a grain boundary, whereas L2 was scanned across a Au particle. The depletion of Au atoms in the dark regions is clearly shown in the concentration profile of Figure 7(b). The Au segregation along grain boundaries is indicated by the Au concentration peak in Figure 7(c). For the Fe-Au-B-N alloy after creep at 60 MPa two line scans were performed at the locations indicated in Figure 7(d). The corresponding concentration profiles of Au, B, and N are indicated in Figures 7(e) and (f). The formation of Au precipitates along grain boundaries and the depletion of Au in the dark region close to grain boundaries are confirmed.

APT was employed on the Fe-Au and Fe-Au-B-N alloys after creep at 100 and 60 MPa, respectively, to accurately measure the segregation to interfaces and the chemical composition of both the precipitates and the matrix which requires high chemical sensitivity and a spatial resolution at the nm scale. Figure 8 illustrates the locations where APT analyses were conducted (where the positions indicated in Figure 8(a) are not directly corresponding to the regions where APT samples were obtained, but illustrate similar positions). Samples that were extracted from the grain boundary region contained either the grain boundary itself or the phase boundary between bulky grain boundary precipitate and the surrounding matrix. The matrix composition captured in these measurements is referred to as “matrix in the depleted zone” in accordance with the SEM and EPMA images that indicate a lower Au content in this region. Further samples were extracted from the grain interior, in safe distance from the depleted zone, containing the thin matrix precipitates and the matrix of the “non-depleted zone.” Table II summarizes

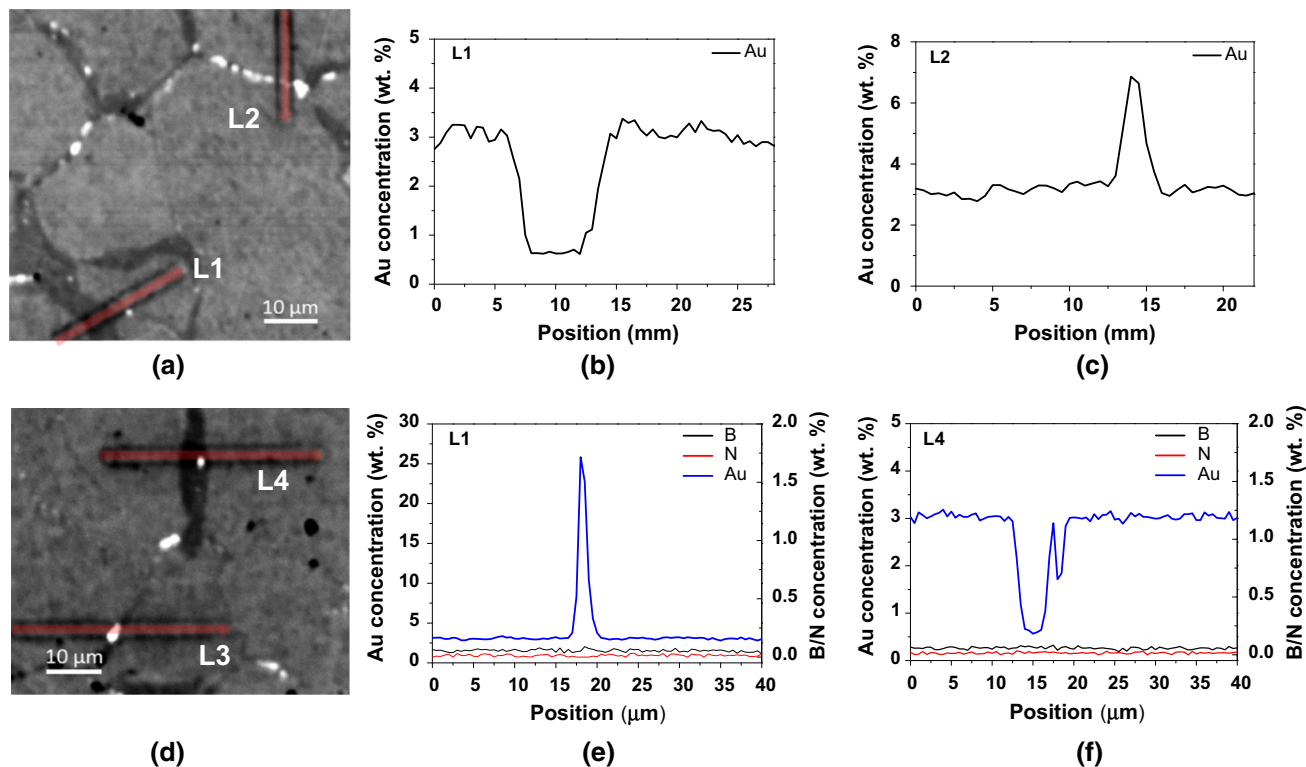


Fig. 7—Elemental concentration profile for (a through c) the Fe-Au alloy after creep at 90 MPa and for (d through f) the Fe-Au-B-N alloy after creep at 60 MPa.

compositions and segregation as quantified by APT. The compositions of the grain interior matrix and the matrix in the depleted zone are almost equal. The contrast change between grain interior and depleted zone at the grain boundary apparent in the SEM and EPMA micrographs is thus not due to different amounts of Au dissolved in the matrix, but caused by the limited spatial resolution of the instruments that cannot resolve the fine matrix precipitates. Coarse grain boundary precipitates and the depleted areas that are free from fine matrix precipitates can be resolved and appear bright and dark with high and low Au content, respectively. The regions containing fine matrix precipitates appear gray in the SEM images and with an intermediate Au content in the EPMA, which is an average of the Au content of the fine precipitates and the matrix. The composition data of the coarse grain boundary precipitates and the matrix as measured by APT are in good agreement with those expected from the Fe-Au phase diagram for binary Fe-Au at a temperature of 823 K (550 °C),^[42] indicating that the phases are in thermodynamic equilibrium. The Au content of the matrix precipitates significantly differs from the Au content of the grain boundary precipitates. This is, however, assumed to be an measurement inaccuracy since the very small size of the matrix precipitates can lead to an underestimation of their Au content in the APT measurement, due to lens and interface blurring effects. More specific, the strong difference in the field evaporation strength between the elements Au and Fe can cause such preferred or

respectively delayed evaporation phenomena especially at phase boundaries, where the composition significantly changes. This can result in a local blurring of the elemental distribution. The fact that the concentration profile depicted in Figure 8(c) shows no plateau indicates that the precipitate is so thin that there is no region free from interface artifacts. In contrast, in the large grain-boundary precipitates a concentration plateau can be measured (Figure 8(b)), which indicates a reliable compositional measurement. The fine matrix precipitates in reality have most likely similar Au contents as the large grain boundary precipitates.

The solutes Au, B, N, C, Mn, and Zn showed enrichment at the internal interfaces. However, Au excess was only detected at grain and not at phase boundaries. Strong variations in the Au excess (a factor of 13) between different grain boundaries (of unknown crystallographic character) were detected. That the B and N contents measured in the matrix by APT are much lower than their nominal compositions suggests that BN precipitation occurred. However, in overall nine successful APT measurements covering $2.5 \times 10^6 \text{ nm}^3$ not a single BN precipitate was detected. The interface segregation of B and N was always rather weak, of film-like morphology and the elemental ratios were significantly different from the stoichiometric 1:1 composition of BN. There is an excellent agreement of the Au content in the depleted zone as determined by EPMA and APT. This allows us to calculate a volume ratio of the fine matrix precipitates in the grain interior, based on the matrix and precipitate composition as

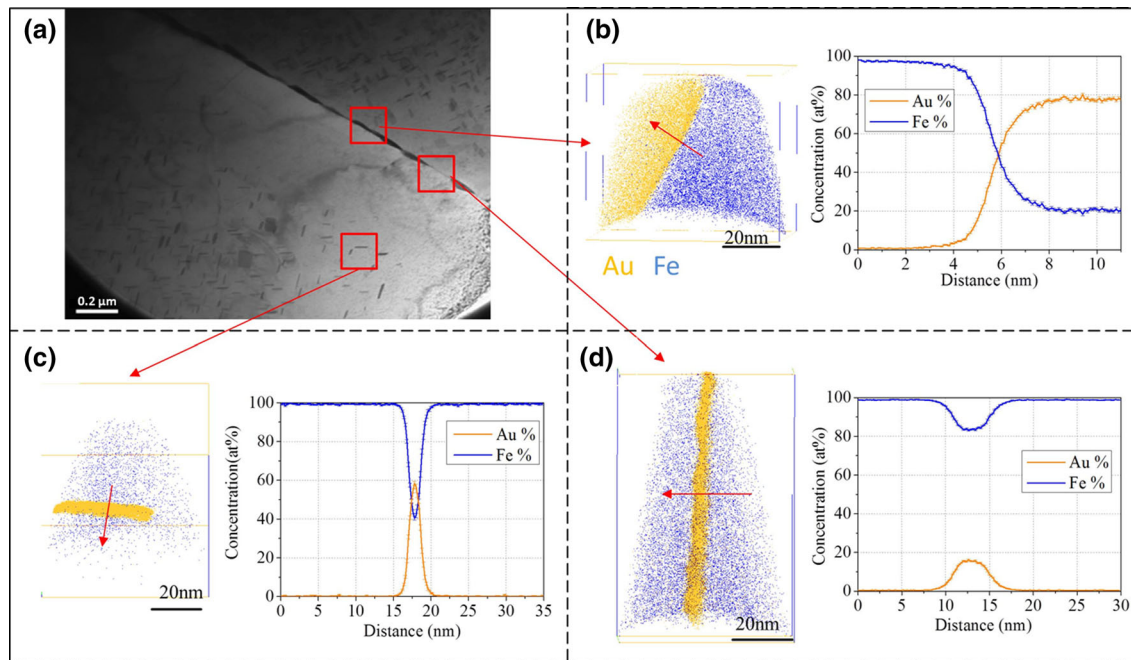


Fig. 8—APT data of the Fe-Au-B-N system after creep at 60 MPa, showing (b) a large grain boundary particle, containing up to 80 at. pct Au (c) a small matrix particle with at least 60 at. pct Au; (d) a high-angle grain boundary, showing Au segregation with local concentrations of 15 at. pct Au. All elements except of Fe and Au remain below 1 at. pct concentration and were removed from the concentration plots. Note that the positions indicated in *a* are not directly corresponding to the regions where APT samples were obtained, but illustrate similar positions.

Table II. Chemical Composition of Matrix and Precipitates Together with the Grain and Phase Boundary Segregation in the Fe-Au-B-N Alloy After Creep at 60 MPa as Measured by Atom Probe Tomography with Balance Iron

Compositions in Wt pct	Au	B	N	C	Mn	Zn
Matrix in grain interior	0.81	—	0.007	0.04	0.023	0.01
Matrix in depleted zone	0.67	0.002	0.001	0.000	0.019	0.35
Precipitates in matrix	80.47	0.003	0.005	0.024	0.029	0.21
Precipitates at grain boundaries	91.61	0.001	0.001	0.001	0.036	0.15
Interface excess in atoms/nm ²						
Grain boundary #1	2.34	0.09	0.02	1.03	0.02	0.03
Grain boundary #2	31.12	0.21	—	0.72	0.06	0.22
Phase boundary	—	0.09	0.03	0.38	0.17	0.54

“—” marks values below the detection limit (10 ppm). The much lower Au content in the matrix precipitate compared to the grain boundary precipitate is most likely an APT size artefact.

determined by APT and the average composition in the grain interior as determined by EPMA. The volume fraction of fine matrix precipitates is estimated to be around 2.4 pct.

IV. DISCUSSION

A. Creep Cavitation Mechanism

Both the fractograph of the rupture surface and the micrographs of cavities and microcracks shown in Figures 3 and 4 indicate that intergranular failure is the dominant failure mode during creep deformation of the current material. Clear indications for healing of creep cavities by Au precipitation are: (1) The Au precipitation is strongest for the grain boundaries most sensitive to creep damage (*i.e.*, those perpendicular to

the loading direction). (2) The shape of the precipitates at the grain boundaries most sensitive to creep damage is irregular, reflecting the same shapes as the creep cavities. (3) In partially filled creep cavities the precipitates generally make contact with both grains on either side of the creep cavity (see Figures 3 and 4 and Reference 22), indicating that the Au precipitation is responsible for the filling of the creep cavity.

The formation of creep damage at high temperatures is schematically shown in Figure 9(a). In the undeformed initial state, the combination of an applied load and a high temperature generates excess vacancies at the grain boundaries perpendicular to the tensile axis.^[38] These excess vacancies will continuously migrate through the matrix toward the grain boundaries oriented along the tensile axis (acting as sinks). This vacancy flow will gradually distort the microstructure,

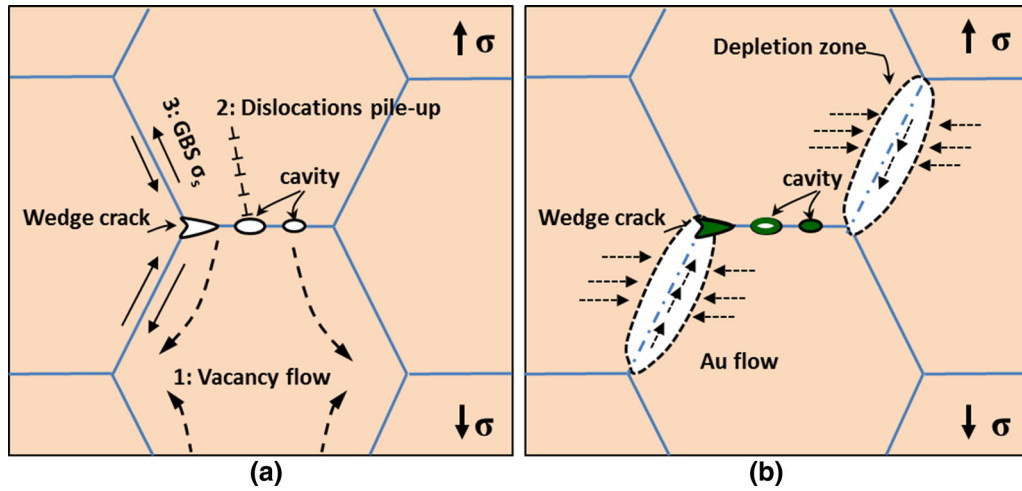


Fig. 9—An illustration of (a) the formation of damage during creep (b) the self-healing of creep damage by Au precipitation.

leading to grains that become elongated along the tensile direction. In addition to the vacancy flow, the excess vacancies may form vacancy clusters at the grain boundaries. When these clusters reach a critical size, a stable creep cavity is formed (nucleation), that will subsequently continue to grow as long as the load is kept constant. At relatively high stresses and low temperatures, creep deformation occurs by the motion of dislocations, including gliding and nonconservative motion, *i.e.*, climbing. The stress concentration associated with dislocations pile-up against obstacles can result in the cavity nucleation along, particularly, transverse grain boundaries. When plastic deformation takes place, additional shear stresses are generated along the grain boundaries that are oriented along the tensile axis. As illustrated in Figure 9(a), these stresses are localized at triple points, where wedge cracks are expected to be formed.

The nucleation of creep cavities by the agglomeration of excess vacancies has been described by Raj and co-workers.^[43] The critical radius for the nucleation of a creep cavity is $r^* = 2\gamma \sin \alpha / \sigma_n$, where γ is the surface energy, $\sigma_n = \sigma \cos \theta$ the stress component normal to the GB and α is the opening angle for the lens-shaped creep cavity ($\alpha \approx 75$ deg for clean surfaces in metals). Using the surface energy for pure Fe^[44] of $\gamma = 2.48$ J/m² a critical radius of $r^* \approx 50$ nm is obtained at a normal stress of $\sigma_n = 100$ MPa. The corresponding energy barrier for nucleation of a creep cavity amounts to $\Delta G^* = (8\pi/3)(2 - 3 \cos \alpha + \cos^3 \alpha)(\gamma^3 / \sigma_n^2)$. In agreement with the present experimental observations, the creep cavity nucleation rate $\dot{N} \propto \exp(-\Delta G^*/RT)$ is maximal for grain boundaries oriented perpendicular to the applied stress ($\sigma_n = \sigma$). Furthermore, it can be seen that the creep cavity nucleation rate is sensitive to local variations in the surface energy. The heterogeneous nature of the grain boundary cavitation indicates that their growth is constrained by creep flow of the surrounding grains.

From the stress exponent $n \approx 2$ observed for the Fe-Au and Fe-Au-B-N alloys, it can be deduced that

grain boundary sliding contributes to the plastic deformation.^[35] Grain boundary sliding can lead to a stress concentration at triple points. When the stress concentration exceeds the cohesive strength of the grain boundary, wedge-cracks can be nucleated.^[2,45] The vacancy accumulation, dislocation pile-up, and grain boundary sliding theories account for the nucleation of cavities and wedge-type microcracks formed during creep, respectively, which are observed in Figures 3 and 4. The appearance of subgrains (Figure 6) confirms the non-uniform creep flow by grain boundary sliding, accommodated by dislocation climbing and gliding. According to a study by Crossman and co-workers,^[46] the contribution of grain boundary sliding to the total strain rate ranges from 15 to 50 pct.

B. Self-healing Mechanism

In the alloys studied, solute Au atoms have a strong tendency to segregate from the homogenized Fe-based matrix. Due to the large size difference between Au and Fe precipitation can only occur at defect sites. In a previous study, we have demonstrated that (1) the defects induced by low-temperature tensile deformation before aging act as a trigger for the Au precipitation^[19,21] and (2) that Au easily segregates to a free surface at high temperatures.^[20] The observed precipitation behavior at a free surface is in line with other observations in a wide range of metal alloys.^[47] No significant internal Au precipitation takes place in the undeformed samples. The site-specific Au precipitation at defect sites provides a high potential for the solute Au atoms to act as efficient healing agents for the micro-cavities and cracks formed during creep at high temperatures.

The autonomous healing mechanism observed is schematically shown in Figure 9(b). We have experimentally observed that the creep cavities formed along grain boundaries have been filled (either fully or partially) by Au precipitation (Figure 3). The irregular geometry of the Au precipitates is attributed to the

allotriomorphic growth on the damage surface of the pore. Both the size and the shape of the Au deposit clearly indicate that there must have been a pore first which was filled by the Au atoms, rather than the Au precipitate to form on an intact grain boundary. The spatial distribution of the Au precipitates is closely correlated with the creep damage. Au precipitates are preferentially formed at (1) grain boundary triple-point junctions, where wedge cracks are preferentially formed due to the stress concentration by grain boundary sliding; (2) grain boundaries oriented perpendicular to the tensile stress (Figures 3 and 4), where the energy barrier for the nucleation of creep cavities is minimum. It is worth noting that dislocations and the subgrain boundaries formed during creep can also act as the nucleation sites for the Au precipitates. In this case, the precipitates are formed as nanometer-sized disk-shaped particles within the matrix (Figure 5(a)). From the fact that the grain boundary precipitates grow under consumption of these fine matrix precipitates it can be concluded that the former ones are thermodynamically preferred. The difference in the particle stability is expected to be related to a difference in strain energy and surface energy. Fine matrix precipitates on well-defined crystallographic planes are often coherent or semi-coherent what goes along with significant coherency strains in the surrounding matrix, while larger grain boundary precipitates are often incoherent, what can be energetically favorable due to a reduction of strain energy.

In our alloys, the site-selective Au precipitation on the creep cavity surface accounts for the improved creep lifetime. The solute Au atoms demonstrate a higher efficiency to extend the lifetime compared to solute Cu atoms. This is attributed to a stronger preferential precipitation on the damage sites. During creep at high temperatures, the initially uniformly dissolved Au atoms will move by combined grain-boundary and volume diffusion. The solute Au atoms are expected to first segregate to the free creep cavity surface and subsequently form an Au-rich precipitate that continues to grow until the cavity is completely filled. It is interesting to note that the larger atomic radius of Au (in comparison with Fe matrix) is beneficial in the filling rate: due to the size difference less atoms are required to fill the open volume.

Boron and nitrogen are widely used alloying elements to improve the mechanical properties of steels. In the case of Fe-Au alloys, the addition of B and N does not alter the site-specific features of the Au precipitation. According to the present APT results, B and N are neither enriched in the Au precipitates nor do they significantly segregate to the phase boundaries. The homogeneous film-like distribution of B and N at the grain boundaries that was seen in all APT volumes containing a grain boundary and the absence of a 1:1 elemental ratio characteristic for BN means that B and N in large parts of the interface only segregate but do not precipitate as BN compound.^[48] These observations indicate that the preferential precipitation of Au to creep cavities dominates the healing reaction and the addition of B and N does not seem to be crucial for this effect in

this alloy system. In our previous study, the addition of B and N was even indicated to decelerate the Au precipitation.^[19,21] Laha and co-workers, however, found a segregation of B and N on the cavity surface in stainless steels, which resulted in the improved creep properties.^[11,12] Our previous XPS results indicate that B and N have a strong tendency to segregate on the free surface during aging.^[20] The interstitial B and N atoms therefore may also play a role in the self-healing of creep damage and needs further study.

The formation of clearly observable Au-depleted regions (Figures 3, 4, 6, 7) along different grain boundaries than the grain boundaries where creep cavities are formed indicates that (1) Au diffusion is much faster along grain boundaries than within the matrix, (2) volume diffusion is required for a continuous supply of solute Au toward the open volume creep-cavities, and (3) the volume diffusion within the matrix must be significantly faster perpendicular than along the applied tensile stress.

If the volume diffusion was isotropic under the applied stress then one would expect that the Au-depleted regions would be located around the grain boundaries where the creep cavities are formed, as the diffusion length would be shortest. Apparently, this diffusion path is however slower indicating a significant anisotropy in volume diffusion of Au under an applied tensile stress. The presence of an anisotropic volume diffusion under an applied tensile stress can either be a result of the lattice distortions (elastic strain)^[49] or from an anisotropy in the dislocation cell structure responsible for the subgrains.^[50]

C. Self-healing Kinetics

So far, experimental and theoretical studies have focused on the nucleation and growth of either creep cavities^[5,38] or grain-boundary precipitates.^[27,51–53] In the context of self-healing, Karpov and co-workers^[54] simulated the precipitation of BN in open-volume defects. In general, the self-healing kinetics is limited by the relative rates of damage formation and precipitation. In order to evaluate the kinetics of the self-healing process, it is essential to obtain the effective grain boundary and volume diffusion coefficient for Au in the Fe matrix. As limited information is available for the grain-boundary diffusion coefficient of Au in pure iron, we will approximate it by the Fe self-diffusion along grain boundaries. At the studied temperature of 823 K (550 °C) the grain boundary diffusivity in iron amounts to $D_{GB} = 2.4 \times 10^{-14} \text{ m}^2\text{s}^{-1}$,^[55] while the volume diffusivity of Au in iron is estimated to be $D_V = 8.3 \times 10^{-20} \text{ m}^2\text{s}^{-1}$.^[37] The effective volume diffusion of Au in iron can be estimated from the width of the Au-depleted region (measured from the GB). From the SEM (Figure 6) and EPMA (Figure 7) results for the Fe-Au alloy after 185 hour creep (at 90 MPa) a maximum depletion distance of about 10 μm is obtained. For a 1D semi-infinite slab model for diffusion and precipitation the concentration profile of the solute atoms can be expressed as^[56]

$$n(s, t) = n_\infty - (n_\infty - n_1) \exp\left(\frac{1}{\pi} \left(\frac{n_\infty - n_1}{n_0 - n_1}\right)^2\right) \operatorname{erfc}\left(\frac{s}{2\sqrt{Dt}}\right), \quad [2]$$

where s is the distance from the slab interface, n_0 is the solute concentration in the precipitate, n_1 the solute concentration close to the precipitate and n_∞ the nominal concentration far away from the precipitate.

Using the literature value for volume diffusion coefficient of Au in an iron matrix^[37] at 823 K (550 °C) and the time to failure a diffusion length of only $2\sqrt{D_V t} = 0.5 \mu\text{m}$ is obtained. The large difference between the diffusion length and the Au-depletion distance indicates that the effective volume diffusivity D_{eff} in our system is significantly higher than the value reported in the literature. The observed depletion distance would reflect an effective volume diffusivity of $D_{\text{eff}} \approx 4 \times 10^{-17} \text{m}^2\text{s}^{-1}$ for Au in the alloy matrix under applied stress. This increase in diffusivity may originate from both (1) the high density of subgrains formed during creep that create faster pathways for diffusion and (2) the distortion of the lattice structure under applied stress, which is responsible for the discussed directional anisotropy for the volume diffusivity.

Under the condition that the diffusion distance $2\sqrt{D_V t}$ is large compared to the size of the subgrains d_{sg} , the effective diffusion coefficient D_{eff} can be expressed as^[57,58]

$$D_{\text{eff}} = (1 - f)D_V + fD_{\text{GB}}, \quad [3]$$

where f is the fractional contribution of subgrain-boundary diffusion to the Au transport. The geometrical constant f reflects the ratio between the diffusional cross sections for subgrain-boundary diffusion ($S_{\text{GB}} = 2\delta d_{\text{sg}}$) and volume diffusion ($S_V = d_{\text{sg}}^2$). For a (sub)grain boundary thickness of $\delta \approx 0.5 \text{nm}$ and a subgrain size of $d_{\text{sg}} \approx 1 \mu\text{m}$ (Figure 6) estimated values of $f = 2\delta/d_{\text{sg}} \approx 0.001$ and $D_{\text{eff}} \approx 2 \times 10^{-17} \text{m}^2\text{s}^{-1}$ are obtained. This suggests that the formation of subgrains is the dominant factor in the enhanced bulk diffusivity for Au in our alloys under applied stress. The enhanced volume diffusion of Au is beneficial to accelerate the self-healing kinetics since Au atoms in the matrix are transferred faster to the grain boundaries.

D. Fraction of Healed Creep Cavities as a Function of the Applied Stress

In our previous study^[22], the fraction of healed creep cavities was obtained for the Fe-Au alloy from an evaluation of the experimental micrographs, as shown in Figure 10(a). The filling ratio reflects the fraction of creep cavity volume that is repaired autonomously by site-selective Au precipitation. As expected, the filling ratio increases for longer creep lifetimes (when the applied stress decreases). A maximum filling ratio of 78 pct is achieved at the minimum load of 90 MPa. Exposed under load at high temperatures, the site-selective Au precipitation at the cavities takes place

immediately after the nucleation of creep cavities. When the creep cavities are generated at a constant rate and all follow the same behavior in terms of cavity growth and precipitation, then the filling ratio of the creep cavities after creep failure η can be estimated by

$$\eta = \frac{\langle V_p \rangle}{\langle V_c \rangle}, \quad [4]$$

where $\langle V_p \rangle$ is the average precipitate volume and $\langle V_c \rangle$ the average creep cavity volume. When the time to fill a single creep cavity t_h is shorter than the creep lifetime of the sample t_f the filling ratio can be estimated by

$$\eta \approx \frac{t_f - t_h}{t_f} = 1 - \frac{t_h}{t_f}. \quad [5]$$

For a given system, the lifetime generally scales with the applied stress σ as

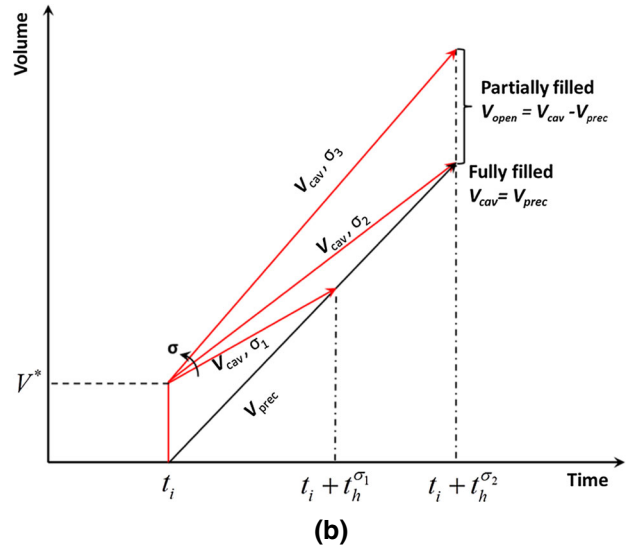
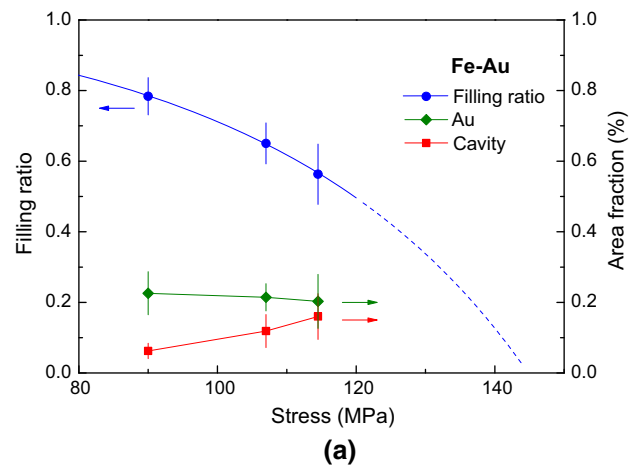


Fig. 10—(a) Experimentally determined areal fraction of unfilled creep cavities, areal fraction of Au precipitates and the resulting fraction of precipitate-filled creep cavities (filling ratio) at different applied stresses for the Fe-Au alloy.^[22] For comparison, the model fit for the filling ratio is shown (see text). (b) Illustration of the time required to fill an individual cavity as a function of the applied stress.

$$t_f = k\sigma^{-n}, \quad [6]$$

where k is a temperature-dependent constant. As observed in Figure 2(a) the exponent amounts to $n \approx 2$ for the Fe-Au and Fe-Au-B-N alloys.

To evaluate the healing time t_h , we assume that (i) at the time of nucleation the volume of the cavity amounts V^* , (ii) after nucleation the cavity volume grows at a constant rate that depends linearly on the applied stress,^[59,60] (iii) when the cavity is formed the solute mass is transported to the cavity at a constant rate.^[51,52] These assumptions lead to a time-dependent creep cavity volume of $V_c(t) = V^* + a\sigma t$ and a precipitate volume of $V_p(t) = bt$. The time to fill an individual creep cavity t_h now strongly depends on the applied stress, as schematically illustrated in Figure 10(b). Solving $V_c = V_p$ provides the healing time:

$$t_h = \frac{(V^*/b)}{1 - (a/b)\sigma} \quad [7]$$

with a filled cavity size of $V_{\max} = V_c(t_h) = V_p(t_h) = V^*/\{1 - (a/b)\sigma\}$. When the applied stress reaches a critical stress of $\sigma_c = b/a$, then the healing time becomes infinite and the creep cavity can never be fully healed. Combining Eqs. [5] to [7] leads to

$$\eta \approx 1 - \frac{c\sigma^n}{1 - \sigma/\sigma_c}, \quad [8]$$

where $c = V^*/bk$. In Figure 10(a) the stress dependence of the measured filling ratio is compared with the model. The fraction of filled cavities decreases with an increase in applied stress as the creep lifetime decreases. After creep failure at 90 MPa, about 80 pct of the damage has been healed by Au precipitation, while at the highest applied stress the filling ratio drops to 56 pct. The experimental data are accurately described by the model. Using a stress exponent of $n = 2$, fit parameters of $c = (1.54 \pm 0.04) \times 10^{-5} \text{ MPa}^{-2}$ and $\sigma_c = 213 \pm 10 \text{ MPa}$ are obtained. With an experimental value of $k = (2.3 \pm 0.5) \times 10^6 \text{ h MPa}^2$ for the Fe-Au alloy (Figure 2(b)) an estimated minimum time of about $V^*/b = ck = 35 \text{ hour}$ is required to fill a cavity at low applied stresses ($\sigma \rightarrow 0$). For the Fe-Au alloy the healing of creep damage is no longer effective beyond an applied stress of about 120 MPa as the filling time becomes longer than the creep lifetime. At an even higher stress level of 144 MPa and beyond the rate of cavity growth is such that the Au diffusion can not keep up with it and no cavity filling takes place at all.

E. Prospects and Outlook

We have demonstrated that solute Au can act as an efficient self-healing agent for creep damage in ferritic Fe-Au and Fe-Au-B-N alloys at high temperatures. The key properties responsible for the observed behavior are (1) a strong chemical driving force for segregation, (2) a high energy barrier for nucleation within the matrix, and (3) a sufficiently high diffusion rate so that the rate at which damage is formed is slower than the rate it is

healed within the studied stress and temperature range. The observed behavior is not expected to be restricted to Au. Other elements with a large atomic radius ($4d$ and $5d$ elements) compared to Fe ($3d$ element) also fulfill the above requirements, and are also potential candidates for autonomous self-healing of creep damage in Fe-based alloys. As other (non-noble) elements are likely to have a tendency to be partially consumed in the formation of additional phases, Au may remain the most effective chemical element for autonomous healing of creep damage in Fe-based alloys and steels.

V. CONCLUSIONS

The creep behavior of high-purity Fe-Au and Fe-Au-B-N alloys was investigated at a temperature of 823 K (550 °C) for different applied stresses. Combined electron-microscopy, EBSD, APT, and EPMA techniques were used to characterize the site-selective segregation process of Au at creep cavities. The main conclusions are as follows:

1. The deformation mechanism is a combination of volume diffusion and dislocation motion modes during creep in the stress range from 60 to 100 MPa. The activation energy of $Q = 257 \pm 15 \text{ kJ/mol}$ was obtained for the solutionized Fe-Au alloy, which agrees well with the activation energy for Au diffusion in bcc Fe.
2. Investigations of creep failed samples indicate an efficient filling of creep cavities by Au precipitates in homogenized Fe-Au and Fe-Au-B-N alloys. Au precipitates nucleate and grow on the free creep cavity surface, which is reflected in the irregular geometry of the formed precipitates. Au precipitates are preferentially formed at the same locations as where creep damage takes place: (1) grain boundary triple points, (2) grain boundaries perpendicular to tensile stress.
3. The site-selective precipitation at creep damage sites indicates that solute Au is an efficient healing agent to heal creep damage in Fe-based alloys. The efficiency to heal creep damage depends strongly on the applied stress. For lower stress levels filling fractions of up to 80 pct have been observed. The observed stress dependence of the filling fraction can be explained by a simple model for the creep cavity growth and the gold segregation rate.
4. The growth kinetics of the healing precipitates is controlled by a combination of fast grain-boundary diffusion and a slower volume diffusion of Au atoms to the creep cavity surface. Au-depleted zones are observed in the vicinity of grain boundaries aligned along the applied load, suggesting an anisotropic volume diffusion of Au in the strained matrix. In the alloys studied a significant subgrain formation is observed by EBSD. These subgrains boundaries are found to have a significant influence on the volume diffusion of Au. It is found that the subgrain boundaries lead to an enhancement of 1 to 2 orders of magnitude compared to the literature

values for volume diffusion of Au in Fe at 823 K (550 °C).

- The addition of B and N does not alter the site-specific Au precipitation at damage sites. B and N segregate to interfaces but no evidence for the formation of BN was found. The preferential Au precipitation at creep damage indicates a high self-healing potential in the Fe-Au-B-N alloy.

ACKNOWLEDGMENTS

This research was financially supported by the innovation-oriented research program (IOP) on self-healing materials of the Dutch Ministry of Economic Affairs, Agriculture and Innovation (IOP Project SHM01017). We thank Marcel Sluiter and Casper Versteyleen for fruitful discussions and Gijs Langelaan for assistance with the development of the creep tester.

OPEN ACCESS

This article is distributed under the terms of the Creative Commons Attribution 4.0 International License (<http://creativecommons.org/licenses/by/4.0/>), which permits unrestricted use, distribution, and reproduction in any medium, provided you give appropriate credit to the original author(s) and the source, provide a link to the Creative Commons license, and indicate if changes were made.

REFERENCES

- M.F. Ashby, C. Gandhi, and D.M.R. Taplin: *Acta Metall.*, 1979, vol. 27, pp. 699–729.
- M. Yoo and H. Trinkaus: *Metall. Mater. Trans. A*, 1983, vol. 14A, pp. 547–61.
- I.W. Chen and A.S. Argon: *Acta Metall.*, 1981, vol. 29, pp. 1321–33.
- P. Shewmon and P. Anderson: *Acta Mater.*, 1998, vol. 46, pp. 4861–72.
- M.E. Kassner and T.A. Hayes: *Int. J. Plast.*, 2003, vol. 19, pp. 1715–48.
- R. Lumley, in *Self-Healing Materials: An Alternative Approach to 20 Centuries of Materials Science*, S. Zwaagvan der, ed., Springer, Dordrecht, 2007, pp. 219–54.
- N. Shinya, in *Self-healing Materials: Fundamentals, Design Strategies, and Applications*, S.K. Ghosh, ed., Wiley, Weinheim, 2009, pp. 219–50.
- M.D. Hager, P. Greil, C. Leyens, S. van der Zwaag, and U.S. Schubert: *Adv. Mater.*, 2010, vol. 22, pp. 5424–30.
- G.Q. Xu and M.J. Demkowicz: *Phys. Rev. Lett.*, 2013, vol. 111, p. 145501.
- K. Laha, J. Kyono, S. Kishimoto, and N. Shinya: *Scripta Mater.*, 2005, vol. 52, pp. 675–78.
- K. Laha, J. Kyono, and N. Shinya: *Scripta Mater.*, 2007, vol. 56, pp. 915–18.
- K. Laha, J. Kyono, and N. Shinya: *Philos. Mag.*, 2007, vol. 87, pp. 2483–2505.
- K. Laha, J. Kyono, and N. Shinya: *Metall. Mater. Trans. A*, 2012, vol. 43A, pp. 1187–97.
- S.M. He, N.H. van Dijk, H. Schut, E.R. Peekstok, and S. van der Zwaag: *Phys. Rev. B*, 2010, vol. 81, p. 094103.
- S.M. He, N.H. van Dijk, M. Paladugu, H. Schut, J. Kohlbrecher, F.D. Tichelaar, and S. van der Zwaag: *Phys. Rev. B*, 2010, vol. 82, p. 174111.
- S.M. He, P.N. Brandhoff, H. Schut, S. van der Zwaag, and N.H. van Dijk: *J. Mater. Sci.*, 2013, vol. 48, pp. 6150–56.
- E. Hornbogen: *Acta Metall.*, 1962, vol. 10, pp. 525–33.
- J. Higgins and P. Wilkes: *Philos. Mag.*, 1972, vol. 25, pp. 599–623.
- S. Zhang, J. Kohlbrecher, F.D. Tichelaar, G. Langelaan, E. Brück, S. van der Zwaag, and N.H. van Dijk: *Acta Mater.*, 2013, vol. 61, pp. 7009–19.
- S. Zhang, G. Langelaan, J.C. Brouwer, W.G. Sloof, E. Brück, S. van der Zwaag, and N.H. van Dijk: *J. Alloys Compd.*, 2014, vol. 584, pp. 425–29.
- S. Zhang, H. Schut, J. Čížek, F.D. Tichelaar, E. Brück, S. van der Zwaag, and N.H. van Dijk: *J. Mater. Sci.*, 2014, vol. 49, pp. 2509–18.
- S. Zhang, C. Kwakernaak, W. Sloof, E. Brück, S. van der Zwaag, and N.H. van Dijk: *Adv. Eng. Mater.*, 2015, vol. 17, pp. 598–603.
- T. Sourmail: *Mater. Sci. Technol.*, 2001, vol. 17, pp. 1–14.
- W.P. Sun and J.J. Jonas: *Acta Metall. Mater.*, 1994, vol. 42, pp. 283–92.
- M. Taneike, F. Abe, and K. Sawada: *Nature*, 2003, vol. 424, pp. 294–96.
- Q. Lu, W. Xu, and S. van der Zwaag: *Philos. Mag.*, 2013, vol. 93, pp. 3391–3412.
- W. Chen and M.C. Chaturvedi: *Acta Mater.*, 1997, vol. 45, pp. 2735–46.
- A. Aghajani, C. Somsen, and G. Eggeler: *Acta Mater.*, 2009, vol. 57, pp. 5093–5106.
- J.T. Armstrong, in *Electron Probe Quantitation*, K.F.J. Heinrich and D.E. Newbury, eds., Plenum Press, New York, 1991, pp. 261–315.
- K. Thompson, B. Gorman, D.J. Larson, B. van Leer, and L. Hong: *Microsc. Microanal.*, 2006, vol. 12, pp. 1736–37.
- B.P. Geiser, D.J. Larson, E. Oltman, S. Gerstl, D. Reinhard, T.F. Kelly, and T.J. Prosa: *Microsc. Microanal.*, 2009, vol. 15, pp. 292–93.
- B.W. Krakauer and D.N. Seidman: *Phys. Rev. B*, 1993, vol. 48, pp. 6724–27.
- O.D. Sherby: *Acta Metall.*, 1962, vol. 10, pp. 135–47.
- J.D. Lubahn and R.P. Felgar, in *Plasticity and Creep of Metals*, J.H. Hollomon, J.E. Burke, B. Chalmers, R.L. Sproull, and A.V. Tobolsky, eds., Wiley, New York, 1961.
- R.L. Coble: *J. Appl. Phys.*, 1963, vol. 34, pp. 1679–82.
- T.G. Langdon: *Philos. Mag.*, 1970, vol. 22, pp. 689–700.
- R. Borg and D. Lai: *Acta Metall.*, 1963, vol. 11, pp. 861–66.
- M.E. Kassner: *Fundamentals of Creep in Metals and Alloys*, Elsevier, Amsterdam, 2008, pp. 11–93.
- D. Lonsdale and P.E.J. Flewitt: *Acta Metall.*, 1984, vol. 32, pp. 869–78.
- B.L. Adams, J.W. Zhao, and D O'Hara: *Acta Metall. Mater.*, 1990, vol. 38, pp. 953–66.
- D.P. Field and B.L. Adams: *Acta Metall. Mater.*, 1992, vol. 40, pp. 1145–57.
- T.B. Massalski, H. Okamoto, P.R. Subramanian, and L. Kaerprak: *Binary Alloy Phase Diagrams*, 2nd ed., ASM International, Materials Park, 1990, p. 368.
- R. Raj and M.F. Ashby: *Metall. Trans.*, 1971, vol. 2, pp. 1113–27.
- H.L. Skriver and N.M. Rosengaard: *Phys. Rev. B*, 1992, vol. 46, pp. 7157–68.
- W.D. Nix, D.K. Matlock, and R.J. Dimelfi: *Acta Metall.*, 1977, vol. 25, pp. 495–503.
- F.W. Crossman and M.F. Ashby: *Acta Metall.*, 1975, vol. 23, pp. 425–40.
- Y. Chen, X.Y. Fang, Y. Brechet, and C.R. Hutchinson: *Acta Mater.*, 2014, vol. 81, pp. 291–303.
- Y.J. Li, D. Ponge, P. Choi, and D. Raabe: *Scripta Mater.*, 2015, vol. 96, pp. 13–16.
- A.J. Ardell and S.V. Prikhodko: *Acta Mater.*, 2003, vol. 51, pp. 5013–19.
- T. Garnier, V.R. Manga, D.R. Trinkle, M. Nastar, and P. Bellon: *Phys. Rev. B*, 2013, vol. 88, p. 134108.
- H.B. Aaron and H.I. Aaronson: *Acta Metall.*, 1968, vol. 16, pp. 789–98.

52. A.D. Brailsford and H.B. Aaron: *J. Appl. Phys.*, 1969, vol. 40, pp. 1702–10.
53. J.J. Hoyt: *Acta Metall. Mater.*, 1991, vol. 39, pp. 2091–98.
54. E.G. Karpov, M.V. Grankin, M. Liu, and M. Ariyan: *J. Mech. Phys. Solids*, 2012, vol. 60, pp. 250–60.
55. G. Stechauner and E. Kozeschnik: *J. Mater. Eng. Perform.*, 2014, vol. 23, pp. 1576–79.
56. C. Zener: *J. Appl. Phys.*, 1949, vol. 20, pp. 950–53.
57. L.G. Harrison: *Trans. Faraday Soc.*, 1961, vol. 57, pp. 1191–99.
58. M. Lübbehusen and H. Mehrer: *Acta Metall. Mater.*, 1990, vol. 38, pp. 283–92.
59. D. Hull and D.E. Rimmer: *Philos. Mag.*, 1959, vol. 4, pp. 673–86.
60. W. Nix, K. Yu, and J. Wang: *Metall. Mater. Trans. A*, 1983, vol. 14A, pp. 563–70.